**Noname manuscript No.**
(will be inserted by the editor)

# Bifurcations of lurching waves in a thalamic neuronal network

**Thomas M. Wasylenko · Jaime E. Cisternas · Carlo R. Laing · Ioannis G. Kevrekidis**

Received: date / Accepted: date

**Abstract** We consider a two-layer, one-dimensional lattice of neurons; one layer consists of excitatory thalamocortical neurons, while the other is comprised of inhibitory reticular thalamic neurons. Such networks are known to support "lurching" waves, for which propagation does not appear smooth, but rather progresses in a saltatory fashion; these waves can be characterized by different spatial widths (different numbers of neurons active at the same time). We show that these lurching waves are fixed points of appropriately defined Poincaré maps, and follow these fixed points as parameters are varied. In this way we are able to explain observed transitions in behavior, and, in particular, to show how branches with different spatial widths are linked with each other. Our computer-assisted analysis is quite general and could be applied to other spatially extended systems which exhibit this non-trivial form of wave propagation.

**Keywords** lurching · bifurcation · RE-TC · lattice

T. M. Wasylenko
Department of Chemical Engineering, Princeton University, Princeton, NJ 08544, USA.
*Present address:* Department of Chemical Engineering, MIT, Cambridge, MA 02139, USA.

J. E. Cisternas
Facultad de Ingenieria y Ciencias Aplicadas, Universidad de los Andes, Santiago, Chile.

C. R. Laing
IIMS, Massey University, Private Bag 102-904 NSMC, Auckland, New Zealand.

I. G. Kevrekidis Department of Chemical Engineering and PACM, Princeton University, Princeton, NJ 08544, USA
Tel.: +1-609-2582818
Fax: +1-609-2580211
E-mail: yannis@princeton.edu

## 1 Introduction

It is well-known that cortical tissue can support traveling waves of activity, both *in vivo* and *in vitro* [11,13,20,22,33,37,38]. Much effort has been dedicated to the mathematical modeling of such waves [5,6,9,10,30,17,31, 26]. Traveling waves observed in continuum mathematical models can travel smoothly, i.e. with a constant profile and speed. When the underlying medium is a lattice (as would naturally arise in cell-level tissue modeling), the perturbation introduced by this discreteness will often cause a slight modulation to the constant traveling shape and wave speed. In contrast, however, a number of models show "lurching" waves, which propagate in a saltatory fashion [34, 36,5,9,14–16]. In this mode of propagation a spatially-localized group of neurons becomes active almost simultaneously; then, after some time, an adjacent group becomes active almost simultaneously, and so on, and so the wave does not have a constant profile (not even approximately). We note that the medium does not have to be spatially discrete for lurching waves to exist. Several authors have analyzed lurching waves in networks of integrate-and-fire [14–16] or integrate-and-fire-or-burst [5] neurons, while others have presented and/or analyzed results from networks of more biophysically-based ordinary differential equation (ODE) models [34,36]. In this paper we consider a model of the latter type, with each neuron described by several smooth ODEs. The fundamental mechanism behind lurching waves in the models [14–16,5,34,36] is post-inhibitory rebound, where a neuron (or group of neurons) fires only after inhibitory input has worn off sufficiently.

Previous analyses of lurching waves have typically made a number of assumptions; for example, that there is an infinite separation of timescales [36], or that neurons fire only once as a wave passes [14–16]. We do not make such assumptions here, and study lurching waves using the concepts and tools of dynamical systems theory. Through careful numerical simulation and the use of continuation techniques we explore the bifurcations of various families of lurching waves, thereby gaining an understanding of the transitions between them.

We consider a one-dimensional network (a lattice) containing a finite number of neurons, the state of each of which is described by a small number of variables. Thus the state of the entire network is described by a high-dimensional vector, and the evolution of this vector is given by a prescribed vectorfield, which depends on various biophysical parameters. Localized waves have activity (for example, elevated voltage) only in a small number of neighboring lattice points at any given time. These waves persist as parameters are changed, resulting in "branches" of solutions. The existence and stability of these branches can be analyzed numerically using bifurcation theory [18,24].

A number of other approaches have been taken to study the propagation of waves in neural systems. For spatially-continuous system models (whether they arise in neuroscience or in other disciplines) moving to a traveling wave frame typically reduces the model to a set of ODEs, and homoclinic orbits of these represent spatially-localized traveling pulses with constant speed [29,10].

If the spatial medium is continuous but periodically modulated in some way, this modulation may be strong enough to cause waves to fail to propagate [8, 4,21,32,23,35]. Alternatively, the wave may travel in a saltatory fashion [7].

Some of our observations and conclusions are consequences of the homogeneity of the lattice and of the neuronal couplings i.e. the *synaptic footprint*. This modeling assumption allows us to simplify the problem and focus on the propagation and the transitions between different types of behavior. We plan to consider more general footprints in the future.

The structure of this article is as follows: In Section 2 we will present the model and demonstrate some of its possible behaviors. In Section 3 we discuss the Poincaré map used to characterize periodic and quasi-periodic waves, and present the continuation method used to trace branches of fixed points of the map. In Section 4 we link the observations of direct numerical integration with the stability/bifurcation and continuation results for periodic solutions, constructing a coherent picture of the transitions observed. In particular, we show nonlinear mechanisms underlying the transition between lurching waves of varying spatial width. We conclude in Section 5 where we discuss our results and outline future work.

## 2 Model

The model we consider consists of two one-dimensional arrays, each representing a layer of neurons (see Fig. 1). One layer consists of excitatory thalamocortical (TC) neurons, each of which is described by variables $v^{\mathrm{TC}}$ (voltage) and $h^{\mathrm{TC}}$ (relative suppressive influence), while the other layer consists of inhibitory reticular (RE) thalamic neurons, described by variables $v^{\mathrm{RE}}$ and $h^{\mathrm{RE}}$.

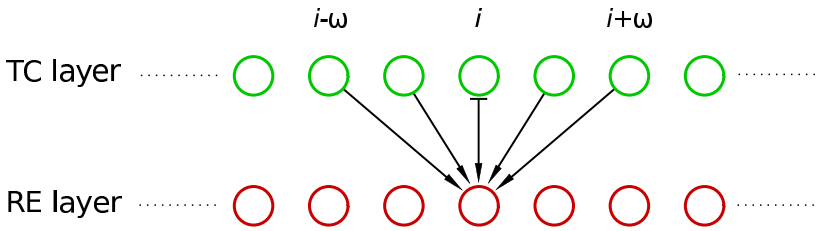


**Fig. 1** Structure of the neural network. In this schematic $\omega = 2$ so that each RE neuron receives excitatory input from the TC neuron at the same site and from the 4 immediately neighboring TC neurons. TC neurons only receive inhibitory input from the RE neuron at the same site.

For each lattice site $i$, where $i \in [1 \dots N]$, there are four differential equations describing the dynamics of the two neurons at that site:

$$C_m \frac{dv_i^{\mathrm{TC}}}{dt} = -g_L^{\mathrm{TC}}(v_i^{\mathrm{TC}} - V_L^{\mathrm{TC}}) - g_{\mathrm{Ca}}(m_\infty(v_i^{\mathrm{TC}}))^3 h_i^{\mathrm{TC}}(v_i^{\mathrm{TC}} - V_{\mathrm{Ca}}) - g^{\mathrm{TC}} s_\infty(v_i^{\mathrm{RE}})(v_i^{\mathrm{TC}} - V_{\mathrm{syn}}^{\mathrm{RE}}), \quad (1)$$

$$\frac{dh_i^{\mathrm{TC}}}{dt} = \epsilon^{\mathrm{TC}} \left[ \frac{h_\infty(v_i^{\mathrm{TC}}) - h_i^{\mathrm{TC}}}{\tau_\infty(v_i^{\mathrm{TC}})} \right], \quad (2)$$

$$C_m \frac{dv_i^{\mathrm{RE}}}{dt} = -g_L^{\mathrm{RE}}(v_i^{\mathrm{RE}} - V_L^{\mathrm{RE}}) - g_{\mathrm{Ca}}(m_\infty(v_i^{\mathrm{RE}}))^3 h_i^{\mathrm{RE}}(v_i^{\mathrm{RE}} - V_{\mathrm{Ca}}) - \frac{g^{\mathrm{RE}}}{2\omega + 1} \left( \sum_{k=-\omega}^{\omega} s_\infty(v_{i+k}^{\mathrm{TC}}) \right) (v_i^{\mathrm{RE}} - V_{\mathrm{syn}}^{\mathrm{TC}}), \quad (3)$$

$$\frac{dh_i^{\mathrm{RE}}}{dt} = \epsilon^{\mathrm{RE}} \left[ \frac{h_\infty(v_i^{\mathrm{RE}}) - h_i^{\mathrm{RE}}}{\tau_\infty(v_i^{\mathrm{RE}})} \right], \quad (4)$$

For future reference this set of autonomous ordinary differential equations can be written as $\dot{x} = f(x)$ where $x \in \mathbb{R}^{4N}$. The positive integer $\omega$ defines the width of the synaptic footprint for connections from the TC layer to the RE layer. Each RE cell receives equally-weighted input from the TC cell at its site, the $\omega$ TC cells immediately to its left, and the $\omega$ TC cells immediately to its right. (Periodic boundary conditions are used.) In this work we considered $\omega = 6$. Each TC cell receives input only from the RE cell at the same site.

The functions that appear in equations (1–4) are smooth and have a sigmoidal shape

$$m_\infty(v) = \left[ 1 + \exp\left( -\frac{(v - \theta_m)}{\sigma_m} \right) \right]^{-1},$$

$$h_\infty(v) = \left[ 1 + \exp\left( -\frac{(v - \theta_h)}{\sigma_h} \right) \right]^{-1},$$

$$s_\infty(v) = \left[ 1 + \exp\left( -\frac{(v - \theta_s)}{\sigma_s} \right) \right]^{-1},$$

$$\tau_\infty(v) = \tau_1 + (\tau_2 - \tau_1) \left[ 1 + \exp\left( -\frac{(v - \theta_\tau)}{\sigma_\tau} \right) \right]^{-1}.$$

with parameters $\theta_s = -20$ mV, $\sigma_s = 2$ mV, $\theta_h = -79$ mV, $\sigma_h = -5$ mV, $\theta_m = -65$ mV, $\sigma_m = 7.8$ mV, $\theta_\tau = -65$ mV, $\sigma_\tau = 4$ mV, $\tau_1 = 1$ ms, $\tau_2 = 80$ ms. Synaptic coupling is assumed to be instantaneous, via the function $s_\infty(v)$. As mentioned, the excitatory TC cells fire by post-inhibitory rebound, i.e. they fire once released from inhibition, as demonstrated in Fig. 2.

The model (1–4) is very similar to that studied by Terman et al. [36], the main difference being that we use instantaneous rather than dynamic synapses. It is important to note that the voltage variables here do not show action potentials, but rather follow the envelope of activity, as spiking currents have

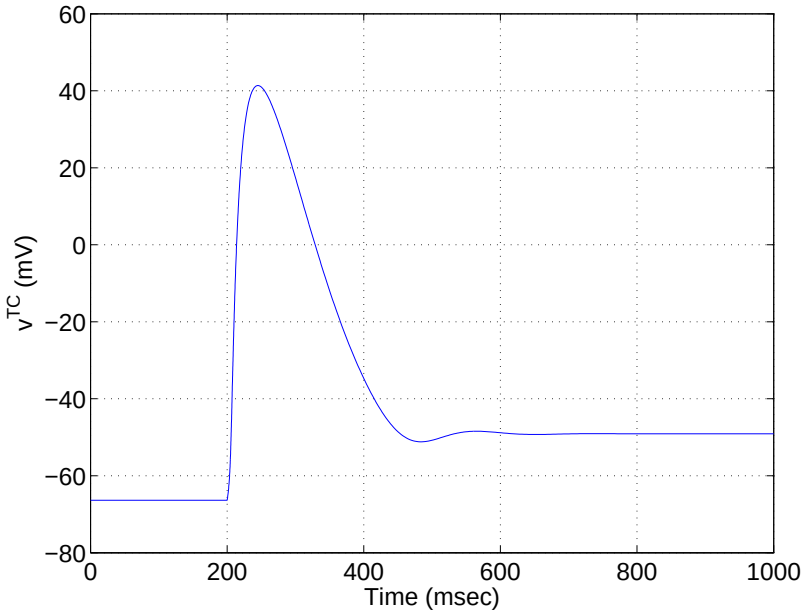


**Fig. 2** A demonstration of post-inhibitory rebound in a single TC cell. Inhibition was released at $t = 200$ msec, resulting in a single action potential.

been removed. Also, using voltage-dependent synapses as we do here (although quite common [34,17]) is a significantly different approach from using event-driven synapses [13–16].

By varying parameters in the model we observed several qualitatively different types of behavior; three representative ones are presented in Figure 3. Figure 3(a,b) shows what we describe as a "smooth" wave, or a "1-lurcher." (The meaning of the parameter $s$ will be explained below.) These activity waves propagate from neuron to neuron, with each cell firing after the cell adjacent to it has fired. The neuron firing times for such a smoothly propagating wave fall on a straight line when plotted in the $x-t$ plane. Moreover, the phase portrait shows that each neuron in the lattice follows the same trajectory when plotted in the $v^{\mathrm{RE}} - v^{\mathrm{TC}}$ phase plane (or in any other two-dimensional projection). In this case one could argue that the discreteness of the propagation medium causes only a "small" perturbation from a continuum traveling wave.

Figure 3(c,d) shows what we call a lurching wave — in this case, a "6-lurcher". As this lurching wave propagates, clusters of six neurons fire (approximately) together, so that the wave of activity "jumps" forward six lattice positions at a time. The characterization "6-lurcher" comes from the fact that neurons in this wave fire in clusters of six. The phase portrait for this solution shows that each neuron in a cluster of six realizes "its own" trajectory, deviating slightly from those of the other neurons in the cluster. However, two

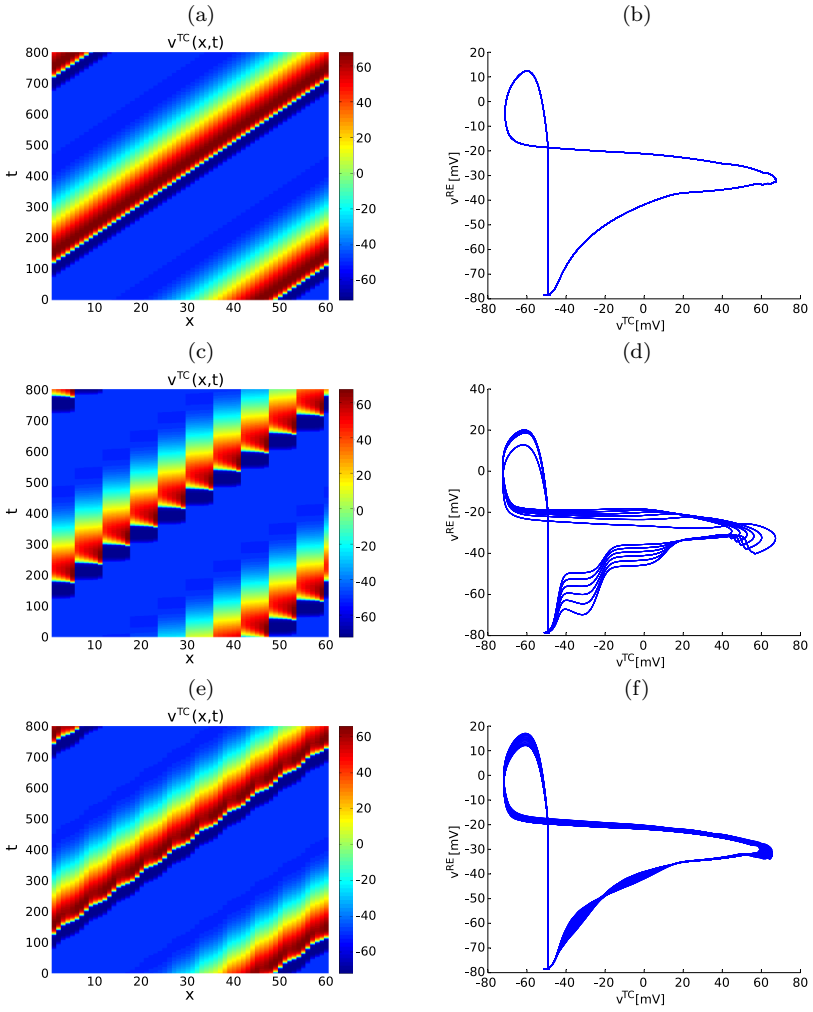


**Fig. 3** Three representative types of behavior of the thalamic neuronal network given by Eqns. (1–4). (a) space-time plot, (b) phase portrait of a smooth wave when $s = 0.6$; (c) space-time plot, (d) phase portrait of a 6-lurcher when $s = 0.8$; and (e) space-time plot, (f) phase portrait of torus B when $s = 0.71$. See text for the meaning of the parameter $s$ and an explanation of the names of these solutions.

neurons that occupy the same position in two different clusters will follow the same trajectory — at different times.

This type of behavior, characterized by a spatiotemporal symmetry where the same phenomenon arises later in time at a position shifted in space, can be considered an extension of what has been given the picturesque name "ponies on a merry-go-round" (POM) [2]. These POM solutions satisfy:

$$u(i,t) = u(0, t - iT/N) \quad i = 0, \ldots, N-1$$

where $T$ is the time required by the entire network to go through one oscillation, $u$ is any one of the variables that describes the state at a single site ($v^{\mathrm{TC}}, h^{\mathrm{TC}}, v^{\mathrm{RE}}, h^{\mathrm{RE}}$), and $i$ the spatial index. Smooth waves (1-lurchers) satisfy this condition.

For $d$-lurching waves, where $d$ is a positive integer, this symmetry can be characterized by

$$u(i,t) = u(i \mod d, t - (i/d)T/N) \quad i = 0, \ldots, N-1$$

where $i/d$ is integer division and the number $i/d$ indicates the cluster to which unit $i$ belongs. Here we have assumed that $N \mod d = 0$.

Figure 3(e,f) shows a third type of representative dynamic behavior. This wave of activity does not propagate smoothly, and although the cells do at first sight appear to fire in clusters, every neuron in the lattice follows its own unique trajectory in the $v^{\mathrm{RE}} - v^{\mathrm{TC}}$ phase plane. This type of behavior, which we argue is *quasi-periodic*, will be discussed in more detail below.

The goal of this work is to understand these different types of traveling wave solutions and, in particular, to characterize the transitions between them as parameters vary. For realistic parameter values, Terman et al. [36] observed a smooth wave solution similar to that shown in Fig. 3(a). For another selection of parameter values they observed a lurching wave solution similar to that shown in Fig. 3(c). The parameters used to obtain these two "representative" solutions were all kept constant, with the exception of $\epsilon^{\mathrm{TC}}$, $g^{\mathrm{TC}}$, $g^{\mathrm{RE}}$ and $V_{\mathrm{Ca}}$. We decided to follow a linear path in ($\epsilon^{\mathrm{TC}}$, $g^{\mathrm{TC}}$, $g^{\mathrm{RE}}$, $V_{\mathrm{Ca}}$) space between these two parameter sets, keeping all other parameters constant. We introduce the non-dimensional parameter $s$ to represent distance along this path, with $s = 0$ corresponding to the smooth wave solution and $s = 1$ corresponding to the lurching wave solution. The four parameters of interest are thus written

$$\begin{aligned}
\epsilon^{\mathrm{TC}} &= 1 + 2s \ , \\
g^{\mathrm{TC}} &= 0.03 + 0.07s \ \mathrm{mS/cm^2} \ , \\
g^{\mathrm{RE}} &= 0.1 + 0.2s \ \mathrm{mS/cm^2} \ , \\
V_{\mathrm{Ca}} &= 120 - 30s \ \mathrm{mV} \ .
\end{aligned}$$

Varying the parameter $s$ will allow us to explore codimension-1 bifurcations involving the stable smooth wave that exists when $s = 0$, the stable lurching wave that occurs when $s = 1$, and possibly other solutions that arise in-between. We find that most of the transitions take place in a narrow range of the parameter $s$. Obviously, the model (1–4) has a large number of parameters, and trying to understand the role of each of them in determining the type of behavior seen is not feasible. By following a (largely arbitrary) 1-dimensional line through parameter space we hope to observe "typical" (codimension-one) bifurcations that would be seen by varying other single parameters alone. In varying $s$ we do not expect to observe all possible bifurcations that could occur in (1–4), but we will be able to link the two main forms of wave propagation seen (smooth and lurching) and detect bifurcations that could be followed as two parameters are varied independently.

All other parameters not yet specified were held constant throughout the investigation. They are $g_L^{\mathrm{TC}} = 0.01$ mS/cm$^2$, $V_L^{\mathrm{TC}} = -75$ mV, $V_{\mathrm{syn}}^{\mathrm{TC}} = 0$ mV, $g_L^{\mathrm{RE}} = 0.2$ mS/cm$^2$, $V_L^{\mathrm{RE}} = -80$ mV, $\epsilon^{\mathrm{RE}} = 2$, $V_{\mathrm{syn}}^{\mathrm{RE}} = -80$ mV, $g_{\mathrm{Ca}} = 1$ mS/cm$^2$, $C_m = 1$ $\mu$F/cm$^2$.

## 3 Methods

In this section we discuss the methods we use to characterize the types of solutions shown in Figure 3, and to follow them as parameters are varied, detecting the associated bifurcations.

### 3.1 Poincaré maps

To characterize the solutions shown in Fig. 3 we use a Poincaré map, defined on a Poincaré section. Such maps are commonly used to study periodic or quasiperiodic behavior [18,24]. Suppose that our system $\dot{x} = f(x)$ has a periodic orbit, $\Gamma$, as shown in Fig. 3 (a), on which the voltage of a specific TC neuron ($v_j^{\mathrm{TC}}$) is equal to a specified value ($p_0$) twice, once with $v_j^{\mathrm{TC}}$ increasing and once with $v_j^{\mathrm{TC}}$ decreasing. Our Poincaré section $\Sigma$ is then defined to be the hyperplane on which $v_j^{\mathrm{TC}} = p_0$. The periodic orbit $\Gamma$ intersects $\Sigma$ twice, at say $y_1^*$ and $y_2^*$, at which $v_j^{\mathrm{TC}}$ is increasing or decreasing, respectively.

The Poincaré map $P : \Sigma \to \Sigma$ is then defined for points $y \in \Sigma$ in a neighborhood of $y_1^*$:

$$y \mapsto P(y)$$

where $P(y)$ is the next intersection of the trajectory starting at $y$ with $\Sigma$, with $v_j^{\mathrm{TC}}$ increasing. The point $y_1^*$ is a *fixed point* of $P$ since $P(y_1^*) = y_1^*$. For later use we define $\Sigma$ to be the set of points $x$ for which $p(x) = v_j^{\mathrm{TC}} - p_0 = 0$. The period of the periodic orbit $\Gamma$ is the time taken for the wave solution to traverse the entire network.

Given an initial point $y_0 \in \Sigma$, the map $P$ can be used to generate a sequence of points using $y_{n+1} = P(y_n)$ for $n = 0, 1, 2, \ldots$. If this sequence repeats after $M$ iterations, i.e. $y_{i+M} = y_i$ and $y_{i+m} \neq y_i$ for $1 \leq m < M$, the solution is referred to as periodic with period $M$. In this case the wave will have to traverse the domain $M$ times before the network returns to the exact same state. Another possibility is that the sequence $y_0, y_1, \ldots$ does not repeat; instead, these points fill a topological circle on $\Sigma$. Solutions of this form are referred to as quasi-periodic.

The spatiotemporal symmetry of the traveling wave solutions of interest allows us to modify the Poincaré map described above. Consider the 3-lurcher solution in Figure 4(a). Using a network with 60 lattice sites, 20 clusters of three neurons each must fire for the wave to traverse the entire network and return to its original position. Rather than wait for the wave to travel all the way around the network, one can instead shift the pulse three sites to the

left (assuming that the wave is propagating to the right) at time zero and then allow the wave to propagate back to its original position. The 3-lurcher solution will then be a fixed point of this operation.

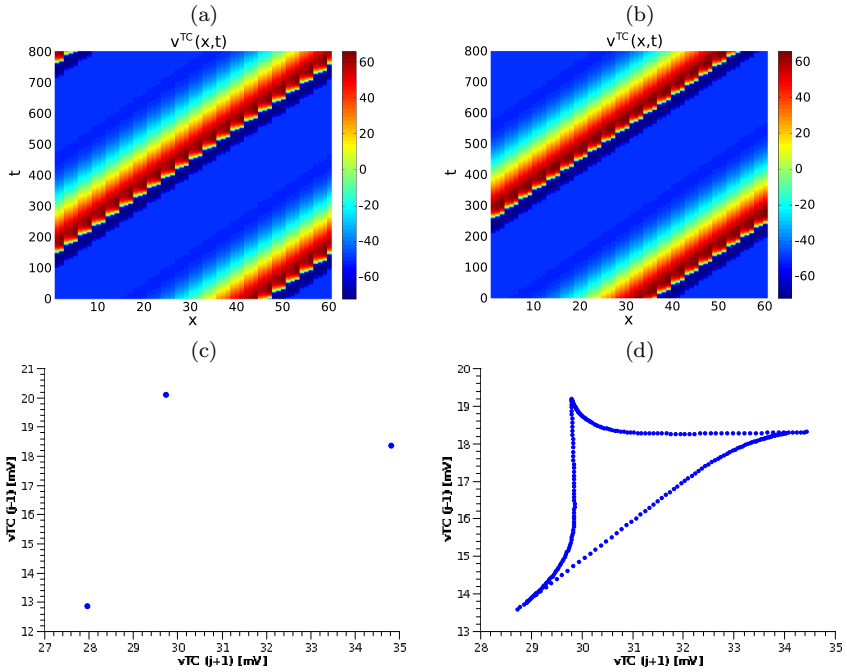


**Fig. 4** A demonstration of the use of Poincaré maps: (a) Space time plots of a 3-lurcher for $s = 0.716$; and (b) torus A for $s = 0.715$; (c) A projection of the Poincaré map $P_1$ of the 3-lurcher for $s = 0.716$; and (d) of the torus A for $s = 0.715$. Note how difficult it would be for the eye to determine this crucial difference between the two top pictures.

We thus define the map $P_d : \Sigma \mapsto \Sigma$ as

$$y \to P_d(y)$$

where $P_d(y)$ is the next intersection of the trajectory starting at $y$ with $\Sigma$, with $v_j^{\mathrm{TC}}$ increasing, *given that the pulse described by $y$ is shifted $d$ positions to the left at time zero*. If $d$ is chosen appropriately based on the properties of the solution being investigated i.e. the cluster size, then a $d$-lurcher will be a fixed point of $P_d$. Its period $\tau$ is defined to be the time it takes the wave to propagate $d$ positions in the lattice.

Using the *shift-and-run* mapping $P_d$ is far more economical than using the map $P$, because the decrease in the period reduces the integration time. Moreover, for a large enough network, the period of the map $P_d$ depends only on the speed of wave propagation, i.e. the time needed for one cluster to fire, while the period of $P$ depends crucially on the actual size of the network. It

should be clear that any solution that is periodic (quasi-periodic) under $P$ is also periodic (quasi-periodic) under $P_d$ and that any solution that is stable (unstable) under $P$ is also stable (unstable) under $P_d$. Note that all of the results shown in this paper were found using the map $P_d$, not $P$.

Figure 4 (c) shows a projection of the Poincaré map $P_1$ for the 3-lurcher shown in panel (a). The projection involves plotting $v_{j-1}^{\mathrm{TC}}$ versus $v_{j+1}^{\mathrm{TC}}$ for points on $\Sigma$, where $v_j^{\mathrm{TC}}$ is used in the definition of $\Sigma$. This projection is used in all subsequent figures in which $P_1$ is plotted, except Fig. 15. Panels (b) and (d) of Fig. 4 show a space-time plot and Poincaré map representation of another solution we found, which we refer to as "torus A." The 3-lurcher appears as three points which form a period-3 orbit of $P_1$: $y_1 \mapsto y_2 \mapsto y_3 \mapsto y_1 \mapsto \cdots$, and each of these points is a fixed point of $P_3$. On the other hand the torus A appears as a set of points that wander in $\Sigma$ and fill a closed invariant curve.

In more mathematical terms the Poincaré map $P_d : \Sigma \mapsto \Sigma$ can be defined as

$$P_d(y) \stackrel{\mathrm{def}}{=} \Phi_{\tau(y)}(S_d(y)),$$

where $S_d$ is a spatial shift of $d$ sites to the left using periodic boundary conditions (which can be implemented using multiplication by a $4N \times 4N$ matrix), $\Phi_\tau(x^0)$ is the solution at time $\tau$ of the differential equation $\dot{x} = f(x)$ with initial condition $x(0) = x^0$, and $\tau(x^0)$ is the smallest positive time for which $p(\Phi_{\tau(x^0)}(S_d(x^0))) = 0$, with $\nabla_x p \cdot f$ evaluated at $x = \Phi_{\tau(x^0)}(S_d(x^0))$ being positive. Thus the map selects transverse crossings of $\Sigma$ at which $v_j^{\mathrm{TC}}$ is increasing. To find a fixed point of $P_d$ one would solve $y = P_d(y)$ for $y$. The period $\tau(y)$ is not an unknown, but is defined to be the time needed for the solution starting at $y$ to return to $\Sigma$, crossing in the appropriate direction. We emphasize that although the map $P_d$ was most useful for computing $d$-lurchers and assessing their stability, the map $P_1$ was used for all the figures showing projections of Poincaré maps (except Fig. 15). Thus, a $d$-lurcher appears as $d$ points in these figures.

The effects of the periodic boundary conditions are worth mentioning here. We use these so that the spatial shift $S_d$ is well-defined, but we choose a domain large enough that the region of active neurons is small relative to the domain size, so that a pulse is largely unaffected by its own "tail" that it effectively sees ahead of it. (See, for example, Figs. 3 and 4.) Thus our results should be correct for solitary pulses traveling on an infinite domain, although possibly with small finite-size corrections.

### 3.2 Numerical integration

Before embarking on a detailed study of the properties of the periodic and quasi-periodic solutions seen above, we used direct time integration to generate a partial summary of the possible stable solutions. Extensive direct numerical simulation was performed using the following protocol. First, we started with a perturbation in the $v_i^{\mathrm{TC}}$ from the (spatially uniform) rest state. This generated both left- and right-traveling waves, but by transiently changing the boundary

conditions it was possible to eliminate the left-traveling wave. After some time to wash out transient behavior, we started recording local maxima and minima (in time) of the spatial average $\langle v_i^{\mathrm{TC}} \rangle$; we stop after some large, fixed amount of simulation time. Then we make a small increment in $s$, resume integration from the last solution shape, wash out transients, and again record local maxima and minima of $\langle v_i^{\mathrm{TC}} \rangle$ for the new value of $s$. We continue until $s = 1$, and then plot the observed local maxima and minima as a function of $s$. For this integration we used a FORTRAN 77 implementation of ODESSA [28], an integrator of stiff ODEs with built-in sensitivity analysis, a feature that will play an important role in the pseudo-arclength continuation discussed below.

Direct time integration will not converge to unstable solutions. However, direct time integration does show the following facts about waves in the neural network: (i) branches of localized waves persist as the parameter $s$ is varied; (ii) changes in stability of one wave may lead to a smooth transition to another wave, or to an abrupt jump to a completely different one; (iii) more than one wave can coexist for some ranges of the parameter $s$, resulting in hysteresis as we move the parameter back and forth across these ranges. The results of these slow sweeps in parameter space are described in Section 4.

### 3.3 Continuation

To obtain a more complete picture of the dynamics of the system we use continuation techniques, which allow one to follow a branch of solutions, irrespective of its stability. By doing this we find unstable branches of solutions, and understand better the behavior of the stable solutions and the ways the stable branches connect with each other.

We are looking for fixed points of the Poincaré map $P_d$ , corresponding to lurching waves with spatial width ("clusters") of size $d$. To implement a continuation algorithm, we rewrite the problem of solving $x = P_d(x)$ as the problem of solving

$$x - \Phi_\tau(S_d(x)) = 0 \tag{5}$$

and

$$p(\Phi_\tau(S_d(x))) = 0 \tag{6}$$

where $x \in \mathbb{R}^{4N}$ and $\tau \in \mathbb{R}$ are unknowns, together with the transversality condition on the intersection of the trajectory with $\Sigma$. In this formulation, Eq. (5) does not explicitly contain the fact that $x$ is in $\Sigma$ — that is given by (6).

Assume that for a particular value of $s$, $s = s_0$, we have found $x_0$ and $\tau_0$ which satisfy (5) and (6) (by using Newton's method, for example). To find the next point on this branch of solutions we define the vector

$$y \stackrel{\mathrm{def}}{=} \begin{pmatrix} x \\ \tau \\ s \end{pmatrix} \in \mathbb{R}^{4N+2}$$

which satisfies

$$G(y) \stackrel{\text{def}}{=} \begin{pmatrix} x - \Phi_\tau(S_d(x);s) \\ p(\Phi_\tau(S_d(x);s)) \\ n(x,\tau,s) \end{pmatrix} = 0 \tag{7}$$

where we explicitly include the dependence on the parameter $s$, and where $n(x,\tau,s)$ is the pseudo-arclength condition:

$$n(x,\tau,s) = \theta_x\ \hat{x}^T(x-x_0) + \theta_\tau\ \hat{\tau}\ (\tau-\tau_0) + \theta_s\ \hat{s}\ (s-s_0) - \Delta\xi \tag{8}$$

where $(\hat{x},\hat{\tau},\hat{s}) \in \mathbb{R}^{4N+2}$ is a normalized tangent to the branch of solutions and $\theta_x,\theta_\tau,\theta_s$ are positive weights which sum to 1. The step size $\Delta\xi$ is approximately equal to the distance in $\mathbb{R}^{4N+2}$ between $(x_0,\tau_0,s_0)$ and the point that we are trying to find.

The system $G(y)=0$ can be solved using Newton iterations: $y^{(k+1)} = y^{(k)} + \Delta y^{(k)}$ where $\Delta y^{(k)}$ is the solution of the linear problem

$$G(y^{(k)}) + \left.\frac{\partial G}{\partial y}\right|_{y^{(k)}} \Delta y^{(k)} = 0$$

and

$$\frac{\partial G}{\partial y} = \begin{pmatrix} \mathrm{Id} - J_\tau S_d & -f(x(\tau;s);s) & -r_\tau \\ \nabla_x p(x(\tau;s)) & \nabla_x p(x(\tau;s))^T f(x(\tau;s);s) & \nabla_x p(x(\tau;s))^T r_\tau \\ \theta_x \hat{x}^T & \theta_\tau\hat{\tau} & \theta_s\hat{s} \end{pmatrix}$$

where $x(\tau;s) = \Phi_\tau(x;s)$, and $J_\tau = \partial x(\tau;s)/\partial x(0)$ and $r_\tau = \partial x(\tau;s)/\partial s$ are the *sensitivities* of the time evolution with respect to initial condition and parameter, respectively. Once Eq. (7) has been solved, the solution is labelled $y_1$, then $x_0,\tau_0$ and $s_0$ in (8) are replaced by $x_1,\tau_1$ and $s_1$, respectively, and Eq. (7) is solved again, this time for $y_2$, and so on.

The computation of the sensitivities just mentioned deserves some comment. Components of the sensitivity with respect to initial condition (once the iteration has converged, these constitute the so-called *monodromy* matrix)

$$J_{\tau;i,j} \stackrel{\text{def}}{=} \frac{\partial x_i(\tau;s)}{\partial x_j(0)} \quad \text{where} \quad x(\tau;s) = \Phi_\tau(x(0);s) \quad , \ i,j \in \{1,2,\ldots,4N\}$$

can be computed "automatically" by ODESSA in the following way: Taking the partial derivative of both sides of the equation $\dot{x} = f(x;s)$ with respect to $x(0)$,

$$\frac{\partial f(x(t;s);s)}{\partial x(0)} = \frac{\partial}{\partial x(0)}\left(\frac{dx(t;s)}{dt}\right)$$

expanding the left hand side using the chain rule and switching the order of differentiation on the right hand side one obtains

$$\nabla_x f(x(t;s);s)\frac{\partial x(t;s)}{\partial x(0)} = \frac{d}{dt}\left(\frac{\partial x(t;s)}{\partial x(0)}\right)$$

or in terms of $J_t$:

$$\frac{d}{dt}J_t = \nabla_x f(x(t))J_t \ .$$

The solution of this homogeneous linear ODE is:

$$J_\tau = \mathrm{Id} + \int_0^\tau \nabla_x f(x(t)) \ dt \ ,$$

and is computed internally by ODESSA.

The evaluation of the sensitivity with respect to the parameter $s$

$$r_{t;i}(x(0);s) \stackrel{\text{def}}{=} \frac{\partial x_i(t;s)}{\partial s} \quad \text{where} \quad x(t;s) = \Phi_t(x(0);s) \ , \ i \in \{1,2,\ldots,4N\}$$

is computed along similar lines: Taking the time derivative of the previous equation gives

$$\frac{d}{dt}r_t = \nabla_x f(x(t;s);s) \ r_t + \frac{\partial f(x(t;s);s)}{\partial s},$$

an inhomogeneous linear ODE that is also solved internally by ODESSA, using the initial condition $r_0 = 0$, in tandem with the computation of $x(t;s)$ and $J_t$. Note that the use of the shift-and-run map $P_d$, and the relatively large number of ODEs involved, preclude the use of off-the-shelf limit cycle continuation/bifurcation codes.

The procedure used here to compute fixed points of the Poincaré map $P_d$ converges for both stable and unstable solutions, assuming a small pseudo-arclength step $\Delta\xi$ is used (so that initial guesses for the solution of Eq. (7) are sufficiently close to the true solution); reasonable care is needed to adjust the numerical tolerances used by ODESSA in order to keep accumulated errors of the time integration small.

The stability of the fixed points of the shift-and-run map $P_d$ can be determined by computing the eigenvalues of its linearization, $J_\tau S_d$. (In [23] a similar "compound" matrix arises as a consequence of an internal symmetry). Fixed points of the Poincaré map always have a trivial eigenvalue 1 associated with the eigenvector $f(x)$; any temporal shift of the periodic orbit $x(t)$ is also a fixed point of $\Phi_\tau(S_d(x))$ although the shifted orbit will not satisfy Eq. (6). The remaining $4N-1$ eigenvalues of $J_\tau S_d$, $\mu_1, \mu_2, \ldots, \mu_{4N-1}$, are the well-known *Floquet multipliers* [24]. These multipliers characterize the growth or decay of small perturbations from the fixed points of Poincaré map $P_d$. If all multipliers satisfy $|\mu| \leq 1$ then the corresponding solution is stable. If there is at least one multiplier outside the unit circle in the complex plane, the corresponding solution is unstable. Bifurcations occur when one or more Floquet multipliers cross the unit circle as parameters are varied. We are only varying one parameter here, so the following bifurcations are expected generically: (i) saddle-node bifurcation: a single multiplier passes through 1, (ii) period-doubling bifurcation: a single multiplier passes through $-1$, and (iii) Hopf (more accurately, Neimark-Sacker) bifurcation: a complex conjugate pair of multipliers passes through the unit circle, with non-zero imaginary parts.

## 4 Results

### 4.1 Numerical integration

Our aim is to understand the transitions involving spatially localized waves that occur as the parameter $s$ is varied. Figs. 3(a,c,e) and 4(a,b) show some of the solutions that the model (1–4) supports. As discussed in Sec. 3, a more complete picture of the *stable* solutions can be gained by systematically varying $s$ while performing integration of Eqs. (1–4). Fig. 5 shows the results of these sweeps, where we plot local extrema (maxima and minima) of the spatial average of the voltages $v_i^{\mathrm{TC}}$. We used long integration times $T = 30000$ for every value of $s$ to remove transients.

Three integration runs were carried out: (i) $s = 0.695 \to 1.0$. In order of observation, the (presumed) attractors seen are: the stable 1-lurcher (or smooth wave, seen in Fig. 3(a)); a quasi-periodic solution (that we call "torus A," see Fig. 4(b)); a second torus (that we call "torus B," see Fig. 3(e)); a 6-lurcher (see Fig. 3(c)); and a 12-lurcher. (ii) $s = 0.735 \to 0.7$. Here, the (again, presumed) attractors observed are: the 3-lurcher; torus A; and a 1-lurcher. (iii) $s = 0.735 \to 0.8025$. Here we start on the 3-lurcher, but then jump to a 6-lurcher. Tori A and B coexist in a narrow range of $s$ values. Torus B has a larger difference between its reported maximum and minimum values of $\langle v_i^{\mathrm{TC}} \rangle$ than does torus A.

Using direct time integration we were able to find six different types of stable solutions. Some of these coexist over ranges of $s$, leading to hysteresis as $s$ is varied in different directions. Although Fig. 5 shows the attractors that we have found, it gives no real indication as to why branches of solutions terminate and/or link to one another as the parameter is varied. The relationship between branches of qualitatively different solutions, and the presence of unstable branches is now explored using continuation, as described in Sec. 3.3.

### 4.2 Continuation

We first present the results of following the 1-lurcher, 3-lurcher and 6-lurcher branches and discuss the bifurcations they undergo; we will then present results regarding the two branches of stable observed tori. We will conclude by presenting a schematic diagram rationalizing the behavior seen in Fig. 5. Note that the shape of the continuation curves obtained depends on the choice of Poincaré section (Eq. (6)), but the location of the bifurcations does not.

The smooth wave (1-lurcher) exists for all $s \in [0, 1]$, and the results of following it are shown in Fig. 6 (only $0.5 \leq s \leq 1$ is shown). This branch is stable for small $s$ and undergoes a Hopf (more accurately, a Neimark-Sacker) bifurcation at $s = 0.702$. The Floquet multipliers of this smooth wave are shown at the bifurcation in Fig. 7 (a), and the magnitudes of some of them are plotted as functions of $s$ in Fig. 7 (b).

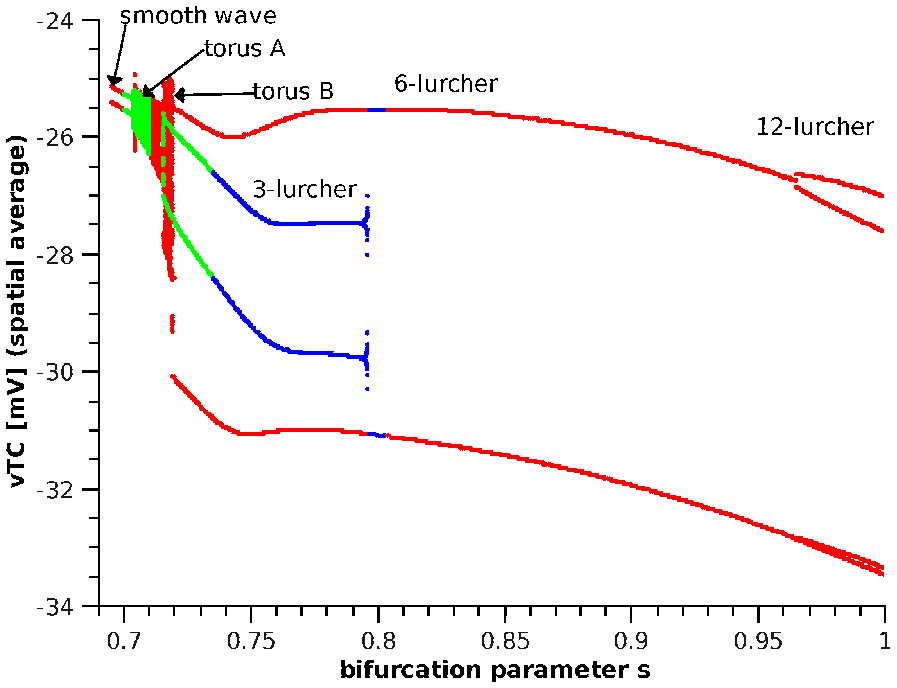


**Fig. 5** The results of direct integration, as $s$ is varied. Three different runs (plotted in different colors) are superimposed. For each branch, both the local minima and maxima of the spatial average of the $v_i^{\mathrm{TC}}$ are plotted. In the first run (plotted in red) $s$ was increased from 0.695 to 1.0. In the second run (plotted in green) we started at $s = 0.735$, on a 3-lurcher, and decreased $s$ to 0.7. For the third run (plotted in blue), $s$ started at 0.735 and was increased to 0.8025. Six different types of stable localized waves were found: 1-lurcher (smooth wave), 3-lurcher, 6-lurcher, 12-lurcher, torus A, and torus B. Up to three such attractors were observed to coexist for certain values of $s$.

The results of following the branch of 3-lurchers (i.e. fixed points of $P_3$) are shown in Fig. 8. We see that two branches are created in a saddle-node bifurcation at $s = 0.7154$, and both branches persist up to $s = 1$. The stable branch created in the saddle-node bifurcation undergoes a subcritical period-doubling bifurcation (we will link this later with the disappearance of an unstable 6-lurcher) at $s = 0.7718$. The limited interval of $s$ values for which a 3-lurcher is stable agrees with the observations in Fig. 5. Note that sub- or super-criticality of all of the bifurcations we find is determined by either linking together different branches of solutions found using continuation, or by direct numerical simulation on either side of the bifurcation.

The results of following the branch of 6-lurchers (i.e. fixed points of $P_6$) are shown in Fig. 9. As in the case of 3-lurchers, two branches (one stable and one unstable) are created in a saddle-node bifurcation at $s = 0.714$. One of them persists up to $s = 1$, while the other terminates at the subcritical period-doubling bifurcation of the 3-lurcher, colliding with the branch of

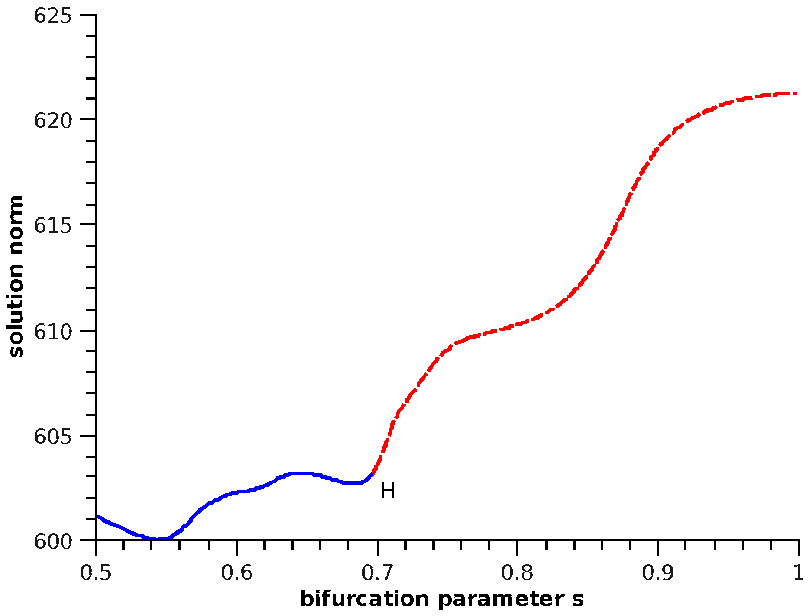


**Fig. 6** Continuation of the smooth wave (1-lurcher). Solid: stable, dashed: unstable. The point H indicates a supercritical Hopf bifurcation.

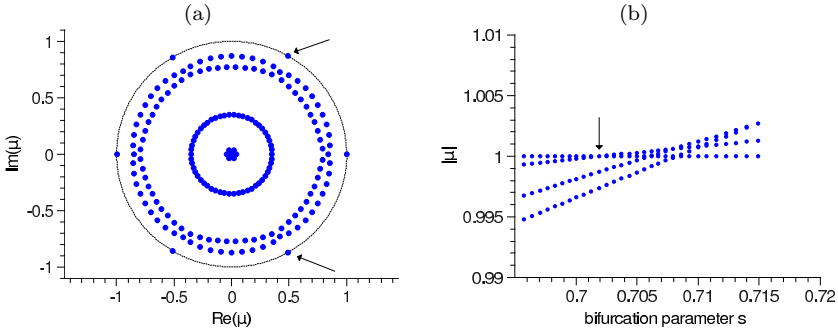


**Fig. 7** (a): Floquet multipliers of the 1-lurcher at the Hopf bifurcation ($s = 0.702$). Arrows point to the multipliers crossing the unit circle. Several more cross at slightly higher values of $s$. (b) Magnitudes of several of the largest magnitude Floquet multipliers as functions of $s$. The arrow indicates the pair of complex conjugate multipliers (indicated in panel (a)) which first leave the unit circle.

3-lurchers at $s = 0.7718$. The stable branch created in the saddle-node bifurcation at $s = 0.714$ undergoes a supercritical period-doubling bifurcation at $s = 0.961$. The unstable branch created at $s = 0.714$ undergoes several saddle-node (sometimes, depending on the number of unstable eigenvalues, saddle-saddle) bifurcations before terminating as $s$ is increased, as shown in

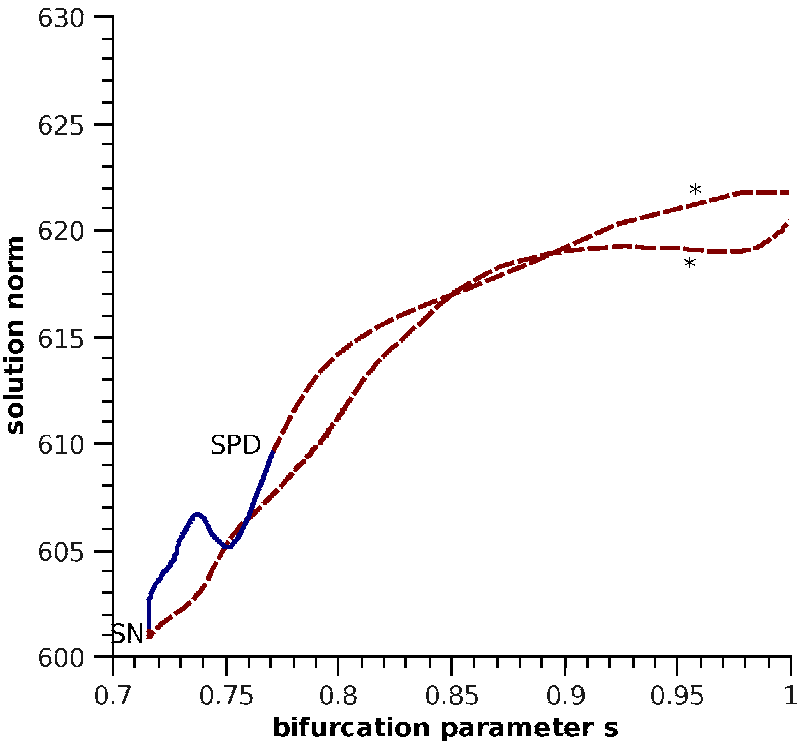


**Fig. 8** Continuation of the 3-lurcher. Solid: stable, dashed: unstable. Points SN and SPD correspond to a saddle-node and a subcritical period doubling bifurcation, respectively. Asterisks along unstable branches indicate points at which additional Floquet multipliers cross the unit circle.

the bottom panel of Fig. 9. Note that there is a small window of $s$ values for which two stable 6-lurchers coexist.

We now discuss in more detail the bifurcations of the branches followed above and their relationship with the quasi-periodic solutions. As seen in Figs. 6 and 7, the smooth wave undergoes a Hopf bifurcation at $s = 0.702$. This bifurcation is supercritical and apparently non-resonant (the two complex multipliers $\mu = \exp(\pm \mathrm{i}\theta)$ exiting the unit circle are not low-order roots of unity), leading to the creation of torus A as $s$ increases through this value; see Fig. 10. As $s$ is increased, torus A increases in size, three "corners" or "folds" start to appear in its projection using $P_1$, and the orbit spends more time near these corners; see Fig. 11. Torus A persists to $s = 0.7153$, which is very close to the value at which the 3-lurcher is created in a saddle-node bifurcation ($s = 0.7154$, see Fig. 8). In fact, plotting torus A at $s = 0.7153$ and the stable 3-lurcher at $s = 0.7154$ using $P_1$ we see that the orbit on torus A spends most of its time in the neighborhood of where the 3-lurcher will appear; see Fig. 12. This strongly suggests that torus A arises "in association with" the saddle-node bifurcation of the 3-lurcher as $s$ is decreased; either the

saddle-node occurs *on the torus itself*, or the torus is formed by global interactions of the stable and unstable manifolds of the saddle 3-lurchers very close to the saddle-node bifurcation marking their birth. The apparent sharp corners of the invariant circle in the picture would argue for the global bifurcation option, but we were not able to find any appreciable hysteresis that would be consistent with this option. For $s$ just less than the saddle-node bifurcation value, a version of "phase walkthrough" [12,27] will occur, i.e. the system will spend a long time seemingly in a 3-lurcher state, but every so often it will "slip" and move to another seemingly stable 3-lurcher state, repeating this pattern.

As seen in Figs 8 and 9, there is a subcritical period-doubling bifurcation on the branch of 3-lurchers at $s = 0.7718$, and this is where one of the branches of 6-lurchers terminates. This is shown more clearly in Fig. 13. In Fig. 14 we plot, in the left column, a space-time representation of the stable 3-lurcher at three different parameter values close to this bifurcation, and in the right column, a similar representation of the unstable 6-lurcher at the same parameter values. We see that as the bifurcation is approached, the 6-lurcher develops two subclusters and becomes more like the 3-lurcher, consistent with the behavior shown in Fig. 13.

As we can see in Fig. 9, the stable 6-lurcher undergoes a period-doubling bifurcation at $s = 0.961$. A real multiplier of $P_6$ passes through $-1$ as $s$ is increased through this value, and the 6-lurcher is unstable beyond this point. Instead, a 12-lurcher is now stable. Thus the bifurcation is supercritical. In Fig. 15 we show both the stable 6-lurcher at $s = 0.96$ and the stable 12-lurcher at $s = 1$.

Neither the continuation nor the direct time integration shed any light on the mechanisms behind the creation or destruction of torus B. This quasiperiodic solution is stable in a narrow range of $s$ values ($0.7011 < s < 0.7185$) and coexists with torus A, and 1-, 3-, and 6-lurchers. It does not seem to interact with either the stable or unstable 6-lurcher. We plot this torus in Fig. 16, where we see that the solution does not develop clusters and/or lurching; it has the appearance of a modulation of a smooth wave. Also, the Poincaré map does not seem to develop "corners" suggestive of global bifurcations, or have regions of particularly high relative density.

We summarize our results with the schematic bifurcation diagram in Fig. 17, which shows how the various solutions we have found link together. In our opinion, the most important observation in this diagram is the link between 1- and 3-lurchers through a quasiperiodic scenario: 1-lurchers lose stability to quasiperiodic solutions, while 3-lurchers are associated with frequency-locking on these same quasiperiodic solutions. Period-6s and 12s are linked to period-3s via period-doublings. We have only considered $\omega = 6$ in this paper, and observed lurchers of period $2\omega, \omega$ and $\omega/2$. This seems to be largely coincidental, as preliminary investigations with other values of $\omega$ show stable lurchers with periods not related to $\omega$ in this way (results not shown). As indicated in the figure, the mechanisms behind the creation and destruction of torus B are as yet unknown.

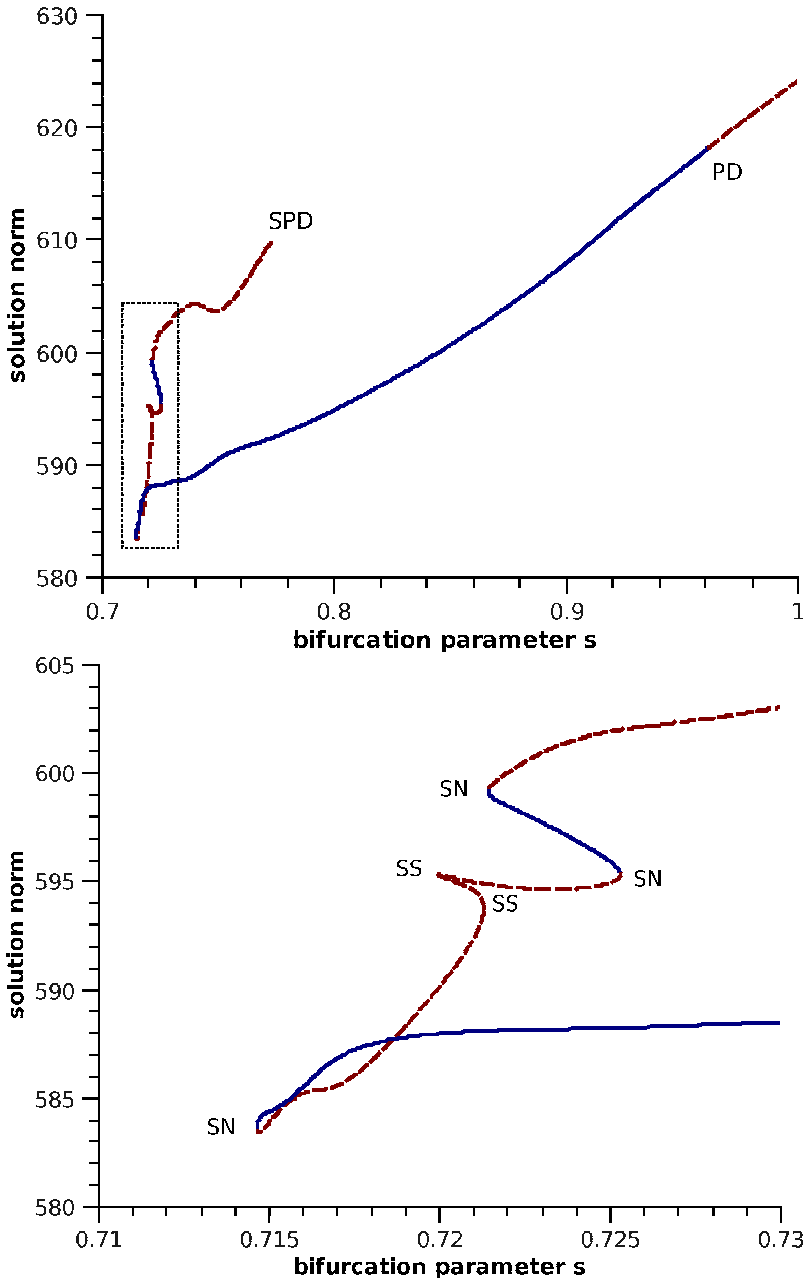


**Fig. 9** Top: continuation of the 6-lurcher. Solid: stable, dashed: unstable. Bottom: a zoom of the rectangle shown in the top panel. SN and SS indicate saddle-node and saddle-saddle bifurcations, respectively, while PD indicates a supercitical period-doubling bifurcation of the 6-lurcher. SPD indicates the termination of the branch of 6-lurchers when the branch of 3-lurchers undergoes a subcritical period-doubling bifurcation (see Fig. 8).

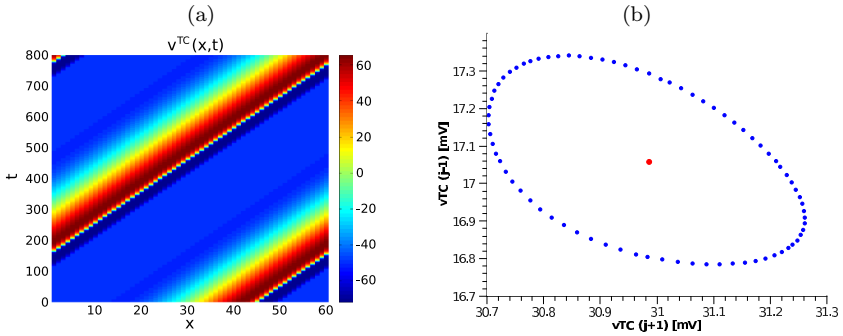


**Fig. 10** Torus A, created in a supercritical Hopf bifurcation of the 1-lurcher, at $s = 0.7025$. (a) Space-time plot. (b) Poincaré map $P_1$ showing the stable invariant circle corresponding to torus A (blue) around the unstable fixed point corresponding to 1-lurcher (red).

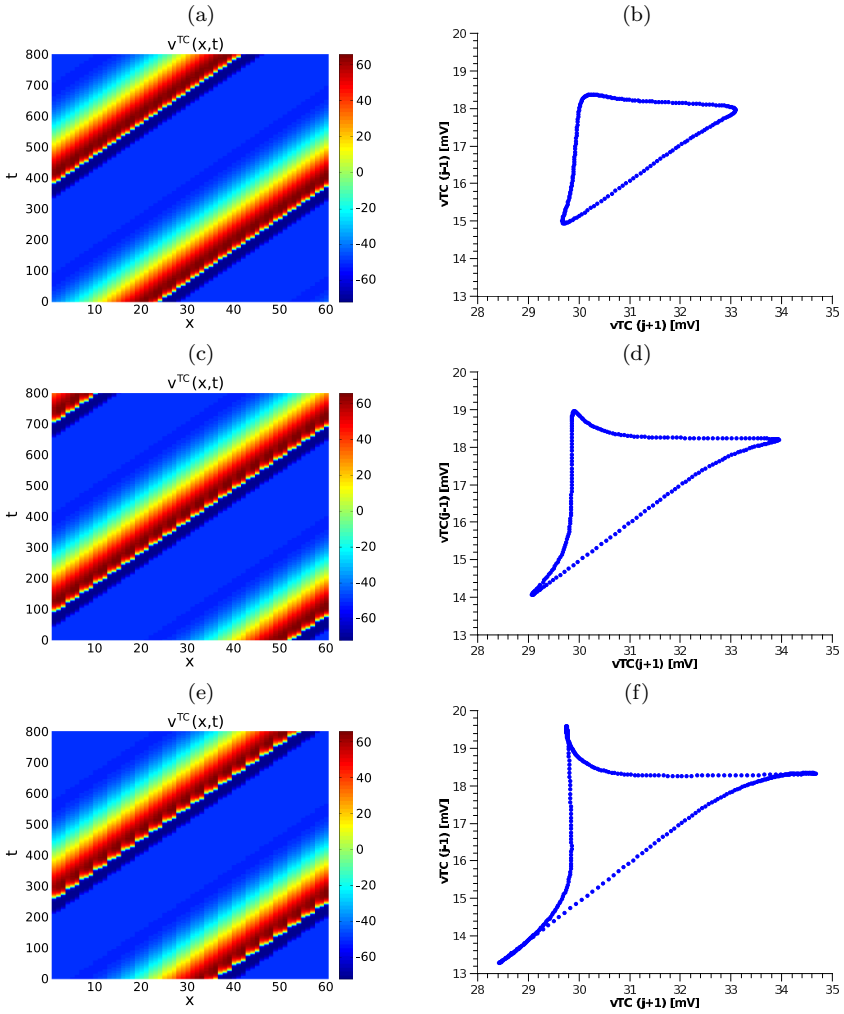


**Fig. 11** Behavior on the torus A as parameter $s$ is increased from top to bottom: $s = 0.705$, $s = 0.71$ and $s = 0.715$. Left column: space-time plots. Right column: Poincaré maps.

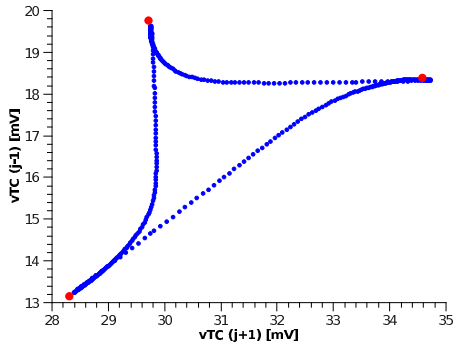


**Fig. 12** Poincaré section representation of the torus A at $s = 0.7153$ (blue) and the stable 3-lurcher at $s = 0.7154$ (red). The solution on the torus A spends most of its time near where the 3-lurcher will be created as $s$ increases.

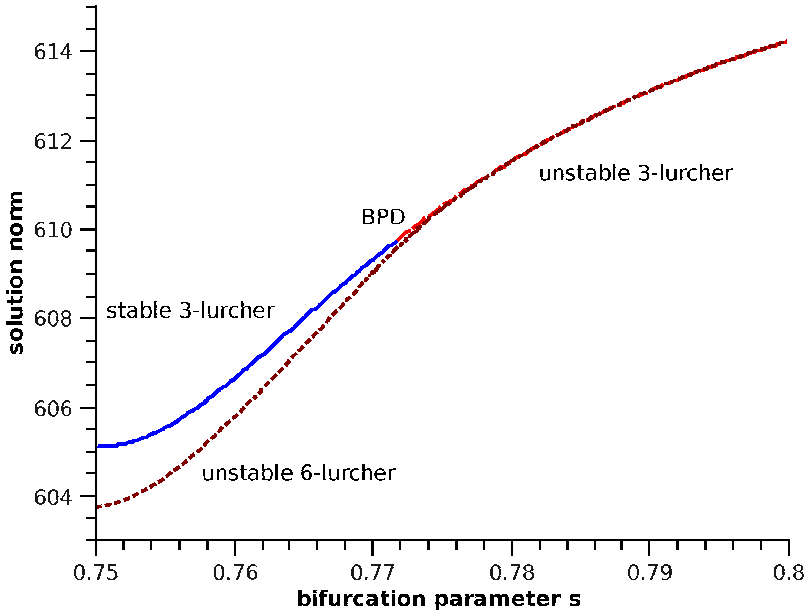


**Fig. 13** The subcritical period-doubling bifurcation of the 3-lurcher. We see the branch of unstable 6-lurchers terminating at the bifurcation.

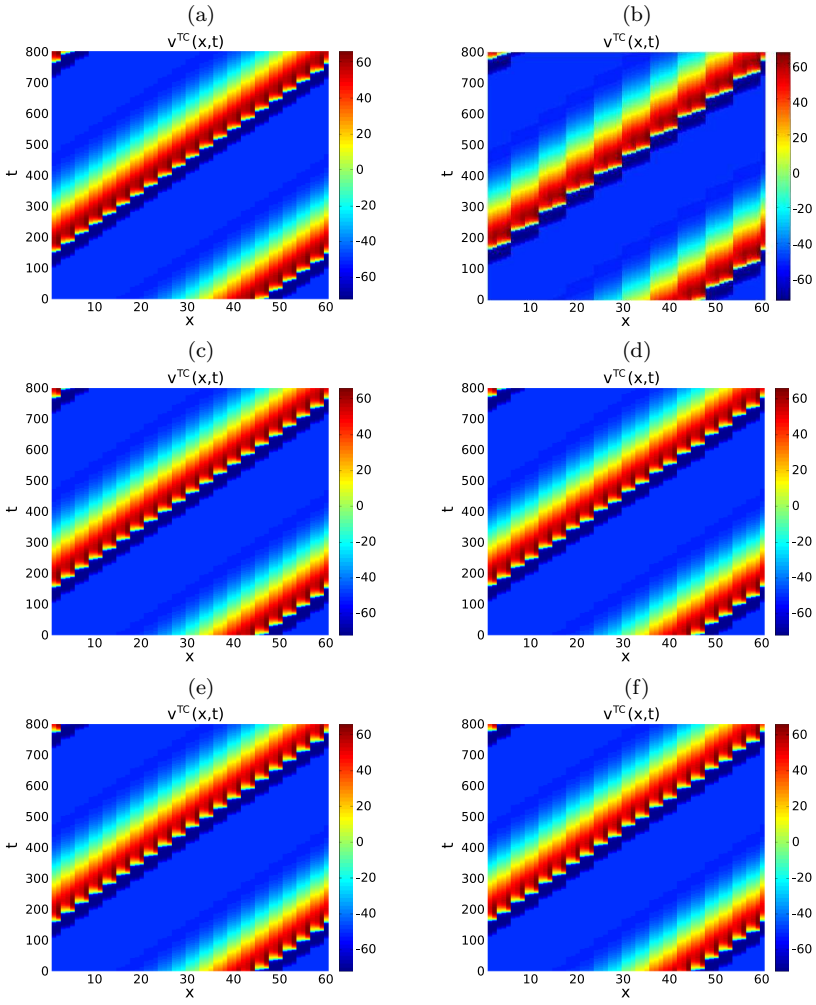


**Fig. 14** Space-time plots of the 3-lurcher and 6-lurcher near the subcritical period-doubling bifurcation shown in Fig. 13. Left column: stable 3-lurcher. Right column: unstable 6-lurcher. Top to bottom: $s = 0.72$, $s = 0.73$, $s = 0.74$. As $s$ increases, the 6-lurcher develops two subclusters and becomes increasingly similar to a 3-lurcher.

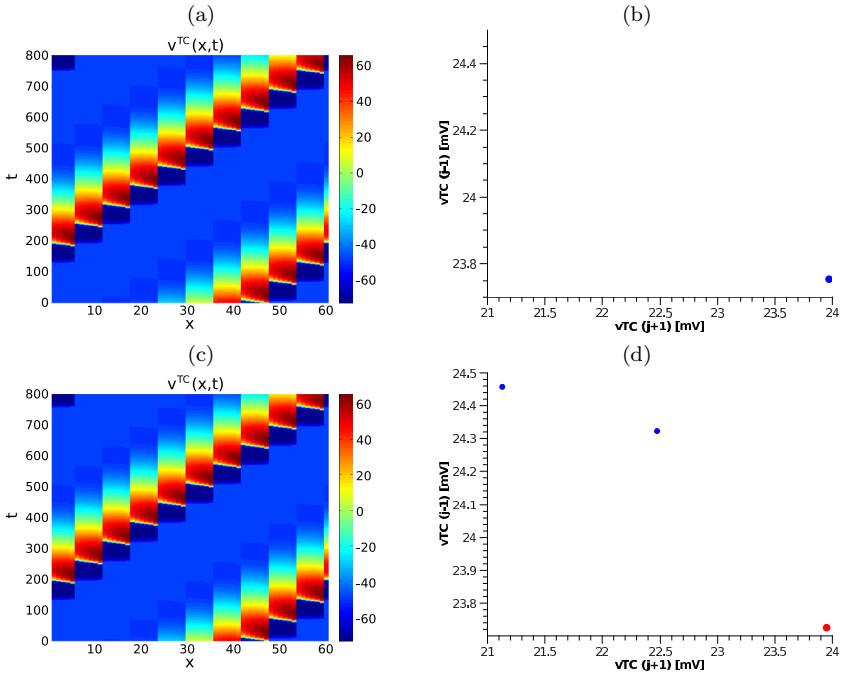


**Fig. 15** Period-doubling of the 6-lurcher. (a): the stable 6-lurcher visualised using a space-time plot at $s = 0.96$ (b): the stable 6-lurcher (blue point) as a fixed point of the Poincaré map $P_6$ ($s = 0.96$). (c): the stable 12-lurcher visualised using a space-time plot at $s = 1$; (d): the stable 12-lurcher (two blue points) and the unstable 6-lurcher (red point) plotted using the Poincaré map $P_6$ ($s = 1$).

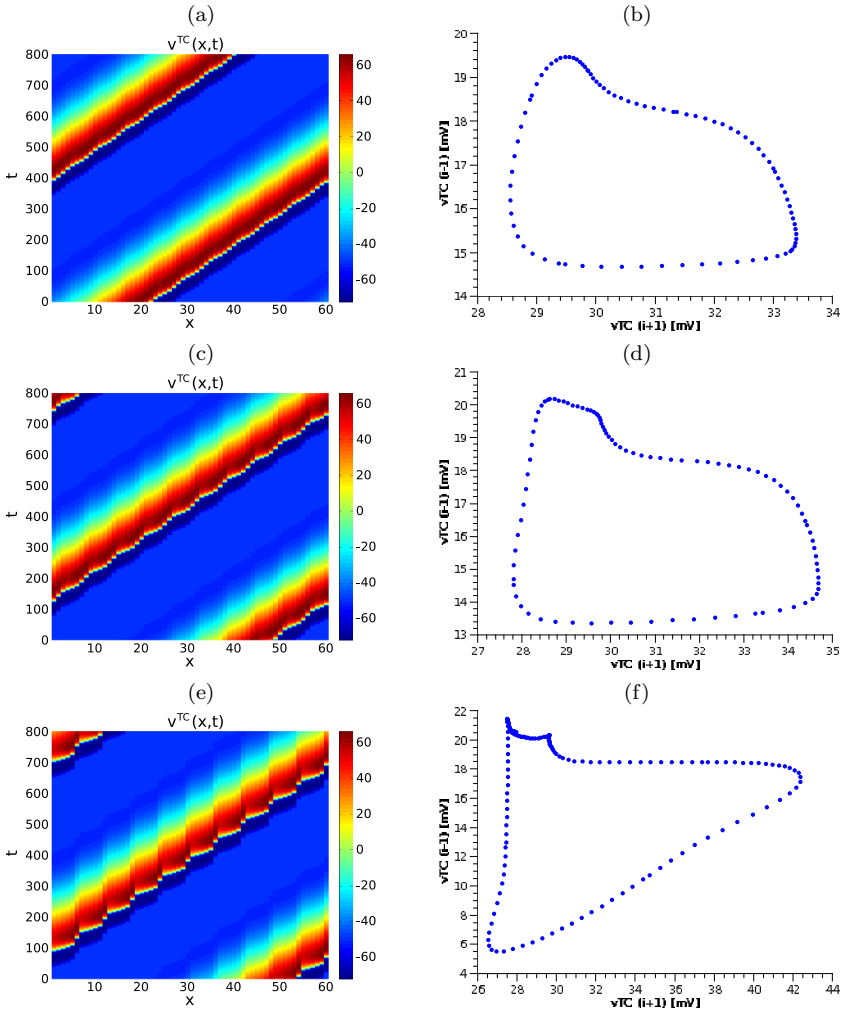


**Fig. 16** Torus B. (a) space-time plot and (b) Poincaré map at $s = 0.7011$; (c) space-time plot and (d) Poincaré map at $s = 0.703$; and (e) space-time plot and (f) Poincaré map at $s = 0.7075$.

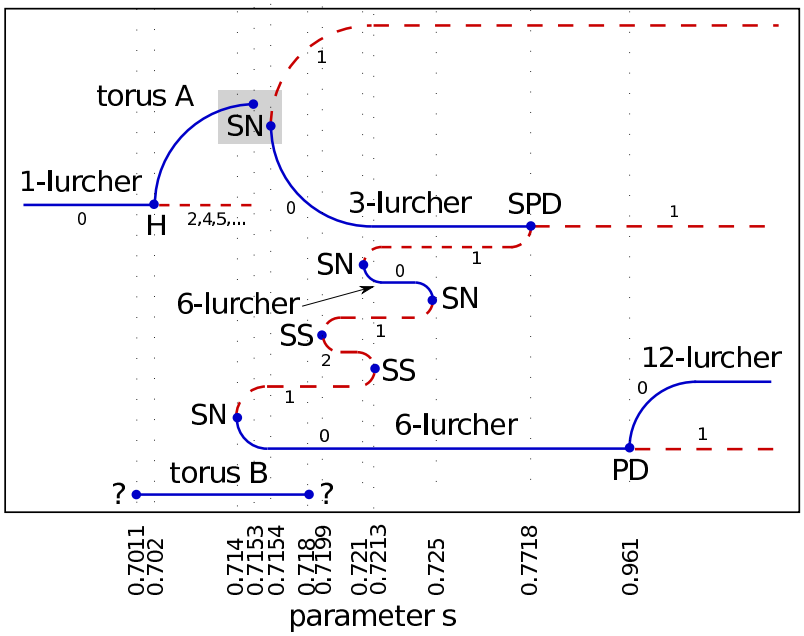


**Fig. 17** A schematic diagram summarizing our current understanding of lurching waves. The horizontal axis is not to scale, and the vertical axis is meant to be qualitative only. Up to three stable solutions coexist for certain values of the parameters. The following symbols are used: H for supercritical Hopf bifurcation; SN for saddle-node bifurcation; SS for saddle-saddle bifurcation; PD for supercritical period-doubling bifurcation; SPD for subcritical period-doubling bifurcation. GB marks a global bifurcation, that would explain the breakup of torus A, associated with a saddle-node bifurcation of periodic orbit. Here "?" indicates a tentative global bifurcation mechanism that deserves further investigation. Numbers along branches indicate the number of Floquet multipliers outside the unit circle.

## 5 Summary and Conclusions

In this paper we have undertaken a numerical investigation of lurching waves in a particular one-dimensional neuronal network. By constructing Poincaré maps, of which lurching waves are fixed points, we have been able to follow these waves as parameters are varied, even when they become unstable. Our current understanding of the relationships between the different lurchers is shown schematically in Fig. 17. We were able to compute stable as well as unstable lurchers, link them to simulations of quasiperiodic waves, quantify their stability and characterize several of their bifurcations. Note that others had already found that lurching waves often appear following a Hopf bifurcation of a smoothly traveling pulse [15]; we also find this (see Fig. 17), but complement it with simulations of the quasiperiodic solutions and by showing the appearance of lurching waves via frequency locking saddle-node bifurcations associated with these tori. Regarding the speed of the different waves that we have found, we note that for all of the branches that we followed, if two or more $N$-lurchers coexist at a particular value of $s$ and one of them is stable, the stable solution had the highest speed. This is commonly seen for smoothly propagating waves [15,16,6], but is in contrast with the results of Coombes for lurching waves [5]. The cause of this discrepancy is at this point unclear, but we point out that Coombes used event-driven rather than voltage-dependent synapses and then assumed a Heaviside firing rate function, and used a different connectivity to us (his model included non-local connections from RE to TC cells) before reducing his two-layer model to one layer.

The computer-assisted analysis presented here is quite general and could be applied to a number of other systems. While the model we studied is spatially discrete, the "shift-and-run" map we introduced could be used for systems in which space is continuous but some aspect of the model is periodically modulated in space. For example, Runborg et al. [35] study a reaction-diffusion system with spatially-periodic modulation of a parameter and observe a Neimark-Sacker bifurcation from a "wiggling pulse" to a "breathing-wiggling pulse." Other neural models having spatially-periodic modulation of a parameter include [3,7]. Also, a number of spatially-homogeneous neural field models show traveling fronts and pulses [25,6], and the ideas presented here could be useful for studying the dynamics of these patterns once biologically-relevant spatial modulations are included [8].

Our computer-assisted analysis goes, we believe, significantly beyond what other authors have deduced in the study of lurching waves [5,14–16,36]. In particular, we have been able to link lurchers of different spatial widths through a quasi-periodic scenario involving tori, frequency locking on them, and possibly global bifurcations associated with frequency-locked solutions. The detailed study of frequency locking, the associated resonance horn boundaries and the global bifurcations indicative of their overlapping constitutes an intrinsically two-parameter scenario [1,19]. Clearly, a two-parameter study starting at the Hopf and important saddle-node bifurcations we found must be performed in order to clarify the dynamics, and, possibly, link what we have observed with

the "isolated" torus B. These rather extensive computations will be the subject of future work; it will be particularly interesting to explore the interaction of this scenario with the discrete variation of the synaptic footprint.

**Acknowledgment:** J.C. wishes to acknowledge the financial support of Universidad de los Andes Grant (Project FAI ING-002-09). The work of I.G.K. was partially supported by the AFOSR and by the US DOE.

## References

1. V. I. Arnold. Small denominators. I: Mappings of the circumference onto itself. *Am. Math. Soc., Transl., II. Ser*, 46:213–284, 1965.
2. D. G. Aronson, M. Golubitsky, and J. Mallet-Paret. Ponies on a merry-go-round in large arrays of Josephson junctions. *Nonlinearity*, 4:903–910, 1991.
3. S. M. Baer and J. Rinzel. Propagation of dendritic spikes mediated by excitable spines: a continuum theory. *J. Neurophysiol.*, 65(4):874–890, 1991.
4. P. C. Bressloff. Traveling fronts and wave propagation failure in an inhomogeneous neural network. *Physica D*, 155(1-2):83–100, 2001.
5. S. Coombes. Dynamics of synaptically coupled integrate-and-fire-or-burst neurons. *Phys. Rev. E*, 67:041910, 2003.
6. S. Coombes. Waves, bumps, and patterns in neural field theories. *Biological Cybernetics*, 93(2):91–108, 2005.
7. S. Coombes and P. C. Bressloff. Saltatory waves in the spike-diffuse-spike model of active dendritic spines. *Physical Review Letters*, 91(2):28102, 2003.
8. S. Coombes and C. R. Laing. Pulsating fronts in periodically modulated neural field models. *Submitted*, 2010.
9. A. Destexhe, T. Bal, D. A. McCormick, and T. J. Sejnowski. Ionic mechanisms underlying synchronized oscillations and propagating waves in a model of ferret thalamic slices. *Journal of Neurophysiology*, 76(3):2049, 1996.
10. B. Ermentrout. Neural networks as spatio-temporal pattern-forming systems. *Reports on Progress in Physics*, 61:353–430, 1998.
11. G. B. Ermentrout and D. Kleinfeld. Traveling Electrical Waves in Cortex Insights from Phase Dynamics and Speculation on a Computational Role. *Neuron*, 29(1):33–44, 2001.
12. G. B. Ermentrout and J. Rinzel. Beyond a pacemaker's entrainment limit: phase walkthrough. *American Journal of Physiology- Regulatory, Integrative and Comparative Physiology*, 246(1):102, 1984.
13. D. Golomb and Y. Amitai. Propagating neuronal discharges in neocortical slices: Computational and experimental study. *J. Neurophysiol.*, 78:1199–1211, 1997.
14. D. Golomb and G. B. Ermentrout. Continuous and lurching traveling pulses in neuronal networks with delay and spatially decaying connectivity. *Proc. Natl. Acad. Sci. USA*, 96:13480–13485, 1999.
15. D. Golomb and G. B. Ermentrout. Effects of delay on the type and velocity of travelling pulses in neuronal networks with spatially decaying connectivity. *Network: Computation in Neural Systems*, 11(3):221–246, 2000.
16. D. Golomb and G. B. Ermentrout. Bistability in pulse propagation in networks of excitatory and inhibitory populations. *Phys. Rev. Lett.*, 86(18):4179–4182, 2001.
17. D. Golomb, X.-J. Wang, and J. Rinzel. Propagation of spindle waves in a thalamic slice model. *J. Neurophysiol.*, 75:750–769, 1996.
18. J. Guckenheimer and P. Holmes. *Nonlinear oscillations, dynamical systems, and bifurcations of vector fields*. Springer-Verlag, New York, 1990.
19. G. R. Hall. Resonance zones in two-parameter families of circle homeomorphisms. *SIAM Journal on Mathematical Analysis*, 15:1075, 1984.
20. X. Huang, W. C. Troy, Q. Yang, H. Ma, C. R. Laing, S. J. Schiff, and J.-Y. Wu. Spiral waves in disinhibited mammalian neocortex. *Journal of Neuroscience*, 24(44):9897, 2004.

21. J. P. Keener. Propagation of waves in an excitable medium with discrete release sites. *SIAM Journal on Applied Mathematics*, pages 317–334, 2000.
22. U. Kim, T. Bal, and D. A. McCormick. Spindle waves are propagating synchronized oscillations in the ferret LGNd in vitro. *Journal of Neurophysiology*, 74(3):1301, 1995.
23. J. Krishnan, K. Engelborghs, M. Bär, K. Lust, D. Roose, and I. G. Kevrekidis. A computer-assisted study of pulse dynamics in anisotropic media. *Physica D*, 154:85–110, 2001.
24. Y. A. Kuznetsov. *Elements of Applied Bifurcation Theory*. Springer-Verlag, Berlin Heidelberg, third edition, 2004.
25. C. Laing and S. Coombes. The importance of different timings of excitatory and inhibitory pathways in neural field models. *Network: Computation in Neural Systems*, 17(2):151–172, 2006.
26. C. R. Laing. Spiral waves in nonlocal equations. *SIAM Journal on Applied Dynamical Systems*, 4(3):588–606, 2005.
27. C. R. Laing and I. G. Kevrekidis. Periodically-forced finite networks of heterogeneous globally-coupled oscillators: A low-dimensional approach. *Physica D*, 237(2):207–215, 2008.
28. J. R. Leis and M. A. Kramer. An ordinary differential equation solver with explicit simultaneous sensitivity analysis. *ACM Trans. Math. Software*, 14:6167, 1988.
29. G. J. Lord and S. Coombes. Traveling waves in the Baer and Rinzel model of spine studded dendritic tissue. *Physica D*, 161:1–20, 2002.
30. M. R. Owen, C. R. Laing, and S. Coombes. Bumps and rings in a two-dimensional neural field: splitting and rotational instabilities. *New Journal of Physics*, 9:378, 2007.
31. D. J. Pinto and G. B. Ermentrout. Spatially structured activity in synaptically coupled neuronal networks: I. traveling fronts and pulses. *SIAM J. Appl. Math.*, 62(1):206–225, 2001.
32. A. Prat and Y.-X. Li. Stability of front solutions in inhomogeneous media. *Physica D*, 186(1-2):50 – 68, 2003.
33. J. C. Prechtl, L. B. Cohen, B. Pesaran, P. P. Mitra, and D. Kleinfeld. Visual stimuli induce waves of electrical activity in turtle cortex. *Proc. Natl. Acad. Sci. USA*, 94(14):7621–7626, 1997.
34. J. Rinzel, D. Terman, X.-J. Wang, and B. Ermentrout. Propagating activity patterns in large-scale inhibitory neuronal networks. *Science*, 279:1351–1355, 1998.
35. O. Runborg, C. Theodoropoulos, and I. G. Kevrekidis. Effective bifurcation analysis: a time-stepper-based approach. *Nonlinearity*, 15(2):491–512, 2002.
36. D. H. Terman, G. B. Ermentrout, and A. C. Yew. Propagating activity patterns in thalamic neuronal networks. *SIAM J. Appl. Math.*, 61:1578–1604, 2001.
37. J.-Y. Wu, L. Guan, and Y. Tsau. Propagating Activation during Oscillations and Evoked Responses in Neocortical Slices. *J. Neurosci.*, 19(12):5005–5015, 1999.
38. J.-Y. Wu, H. Xiaoying, and Z. Chuan. Propagating Waves of Activity in the Neocortex: What They Are, What They Do. *Neuroscientist*, 14(5):487–502, 2008.